Monsoon Tail Rainbands and Tropical Cyclogenesis in the Western North Pacific: Climatology and a Typhoon Jebi (2018) Case Study

CHAEHYEON C. NAM[a] AND MICHAEL M. BELL[b]

[a] *Florida State University, Tallahassee, Florida*
[b] *Colorado State University, Fort Collins, Colorado*

(Manuscript received 13 February 2025, in final form 3 December 2025, accepted 27 January 2026)

ABSTRACT: During the Propagation of Intraseasonal Tropical Oscillations (PISTON) field campaign in the summers of 2018 and 2019 over the western North Pacific (WNP), many tropical cyclones (TCs) exhibited an elongated rainband in the southwestern (SW) quadrant, typically located 500–1000 km from the storm center. We refer to this feature as the "monsoon tail (MT)," hypothesizing that it forms through interactions between the TC circulation and monsoon southwesterlies. A notable case was Typhoon Jebi (2018), where a trailing rainband detached from the main circulation and persisted as widespread convection. This system developed a closed low-level circulation and was designated as Invest 98°W by the Joint Typhoon Warning Center but ultimately failed to undergo tropical cyclogenesis (TCG). Motivated by these observations, we conducted a 40-yr climatological analysis and a case study of Jebi and Invest 98°W. We found that approximately 80% of WNP TCs exhibited at least one MT event under a moderate threshold (5000 km^2 of area, 6 h of duration). Convective asymmetry in the SW quadrant was most strongly correlated with zonal wind shear, while low-level monsoonal flow and thermodynamic factors played secondary roles. Vertical wind shear helped organize asymmetric convection downshear, enabling detached MT structures to resemble incipient disturbances. This dual role of vertical wind shear (VWS) and the preexisting TC circulation—enhancing vorticity and moisture while imposing hostile shear—was evident not only in the Invest 98°W case but also in the climatological analysis using its location as an illustrative example. These findings highlight how MT rainbands may exhibit developmental potential yet remain inhibited from TCG by environmental shear from the parent TC.

KEYWORDS: North Pacific Ocean; Cyclogenesis/cyclolysis; Monsoons; Tropical cyclones

1. Introduction

The western North Pacific (WNP) monsoon (i.e., the Asian–Australian monsoon) and tropical cyclones (TCs) together have enormous societal impacts. Climatologically, rainfall in early summer (May–June) in the Asian monsoon region is due to large-scale monsoon southwesterlies, and much of the rainfall in late summer (July–September) is produced by TCs (Chen and Yoon 2000; Takahashi et al. 2015).

Monsoon circulations and TCs over the WNP are closely intertwined. During the Propagation of Intraseasonal Tropical Oscillations (PISTON) field campaign in boreal summers of 2018–19, we noted that many TCs were accompanied by an elongated convective area to their south.

An interesting example was Typhoon Jebi (2018). On 30 August, when Jebi's center was located near 17°N, 147°E, a pronounced trailing convective band extended southeastward to about 10°N in the southeastern (SE) quadrant (Fig. 1a). During PISTON, the science team informally referred to such trailing convection in the southern quadrants as the "monsoon tail," hypothesizing that low-level convergence between the monsoon southwesterlies and the TC-induced cyclonic circulation supported unusually vigorous convection there.

As Jebi moved northwestward, the elongated convective area south of the storm evolved, gradually extending into the southwestern (SW) quadrant and becoming more widespread within the surrounding monsoon flow (Fig. 1; Fig. S1 in the online supplemental material shows the 6-hourly evolution). By around 1800 UTC 1 September, the convection was no longer contiguous with Jebi's inner-core rainbands yet remained embedded within Jebi's larger-scale circulation. The resulting broad convective region exhibited a closed low-level circulation in satellite analyses on 2–3 September near 16.5°N, 137°E and was monitored by the Joint Typhoon Warning Center (JTWC) as Invest 98°W for potential tropical cyclogenesis. Invest 98°W ultimately dissipated before reaching TC intensity.

The large-scale environments during the 2018 PISTON campaign were reviewed by Sobel et al. (2021), and the coupling between mesoscale convective structures and the large-scale background during PISTON 2018 and 2019 was examined by Chudler and Rutledge (2021). Both studies noted the presence of monsoon tail features but did not investigate them in detail as is done in this study. However, the PISTON team was not the first to document long-lasting trailing rainbands embedded within the monsoonal flow of the WNP. Lee et al. (2012) analyzed long-lived mesoscale convective systems (MCSs) that formed in the outer regions of TCs from distant rainbands—termed "outer MCSs"—and found that approximately 22% of all WNP typhoons exhibit at least one outer MCS during their life cycle. These systems were defined by cloud shield areas

Supplemental information related to this paper is available at the Journals Online website: https://doi.org/10.1175/JCLI-D-25-0092.s1.

Corresponding author: Chaehyeon Chelsea Nam, ccnam@fsu.edu

DOI: 10.1175/JCLI-D-25-0092.1

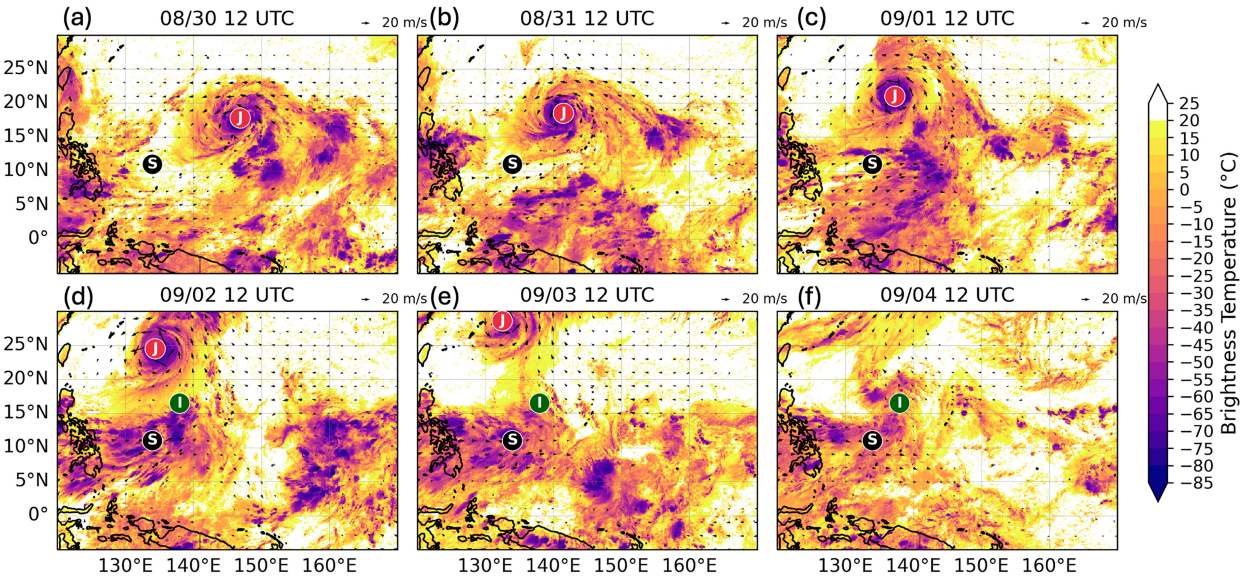

FIG. 1. Daily GridSat-B1 infrared BT over the WNP from 1200 UTC 30 Aug to 1200 UTC 4 Sep 2018, overlaid with 850-hPa wind vectors from ERA5 (showing only vectors with magnitudes greater than 5 m s^{-1}). Typhoon Jebi is marked with a "J," and the location of the R/V (R/V *Thompson*) is marked with an "S." The area labeled "I" denotes a region of persistent, widespread convection that was monitored by the JTWC as Invest 98°W for potential TCG. The 6-hourly evolution of this period is shown in Fig. S1.

colder than −75°C, covering more than 36 000 km^2, located within 1000 km of the TC center, and persisting continuously for at least 6 h. In a follow-up study, Chen et al. (2014a) conducted detailed numerical simulations of an outer MCS during Typhoon Fengshen (2008) and identified a cold pool process beneath a large stratiform rain shield on the downshear side as the key mechanism sustaining continuous convective development in the TC's periphery. Based on these criteria, Invest 98°W would be classified as an outer MCS associated with Typhoon Jebi.

An important question that arises is how frequently tropical cyclogenesis (TCG) originates from outer MCSs or detached monsoon tail (MT) rainbands. Although Invest 98°W did not develop into a tropical cyclone, our observation of MT rainbands during the PISTON campaign—particularly the Invest 98°W case—prompted us to consider whether a detached MT rainband could represent a distinct and underrecognized pathway to TC genesis.

To contextualize this hypothesis, we review the known pathways of tropical cyclogenesis in the monsoonal environment of the WNP. TCG in the WNP is typically associated with five key precursor patterns: monsoon shear lines (SLs), monsoon gyres (GYs), confluence regions (CRs), easterly waves (EWs), and energy dispersion from preexisting TCs (PTCs) (e.g., Ritchie and Holland 1999; Yoshida and Ishikawa 2013). On average, more than 70% of WNP TCs form within the monsoon trough, with interannual variation ranging from 50% to 100% (Molinari and Vollaro 2013). Previous studies identified SL and CR patterns as dominant precursors to TCG in the WNP (Ritchie and Holland 1999; Yoshida and Ishikawa 2013), while Chen et al. (2008) emphasized the significant role of EWs, reporting that over 80% of TCG events were directly or indirectly linked to them—including cases involving interactions between easterly waves and the monsoon trough.

These studies collectively highlight the complexity of TCG in the WNP, where multiple environmental precursors often interact. Notably, EW- and PTC-related patterns frequently coincide with the CR configuration (Yoshida and Ishikawa 2013). Monsoon confluence zones provide abundant moisture, and easterly waves may amplify in these regions via diabatic heating from deep convection (Serra et al. 2008). Barotropic energy conversion may also contribute to the growth of disturbances in these regions through mechanisms such as wave accumulation (e.g., Holland 1995; Sobel and Bretherton 1999; Au-Yeung and Tam 2018). In addition, Zehr (1992) found that localized monsoon westerly wind surges often preceded deep convection in most TCG events over the WNP during 1983–84. Briegel and Frank (1997) similarly reported that approximately 20% of TCG cases in 1988–89 were associated with monsoon westerly surges, which were further enhanced by cyclonic flow from preexisting TCs. Such localized westerly surges—often amplified by existing TC circulations—can support upscale growth and merging processes, potentially enabling outer MCSs to evolve into full-fledged tropical cyclones.

This study is motivated by our PISTON observations of MT rainbands and the case of Invest 98°W and seeks to address the following scientific questions:

- How common is it for TCs in the WNP to exhibit an elongated MT convective area (MT rainband)?
- Under what environmental and TC conditions do such MT rainbands tend to develop and persist?
- How common and likely is it for the MT rainband to lead to subsequent tropical cyclogenesis?

We address these questions through a combination of climatological analysis and case studies focused on MT rainbands, with particular attention to Typhoon Jebi (2018) observed during PISTON. We demonstrate that the MT rainband is a common feature of TCs in the WNP monsoonal region, with its presence and persistence resulting from interactions between TCs and both low-level and upper-level flows. Additionally, we show that although enhanced moisture transport and convective activity are associated with the separated MT rainband, the surrounding environment is generally unfavorable for subsequent TCG due to increased vertical wind shear (VWS).

This paper is organized as follows. Section 2 outlines the data and methods, including both composite- and event-based approaches for identifying MT rainbands. Section 3 presents the climatology of MT features using multiple metrics and sensitivity analyses. Section 4 examines the environmental- and TC-related factors associated with MT convection. Section 5 explores the potential for MT rainbands to lead to TCG, featuring a case study of Invest 98°W and a broader climatological assessment. Section 6 concludes with a summary of key findings and implications.

2. Data and methods

a. Data

Satellite brightness temperature data are from the Gridded Satellite (GridSat-B1) dataset, which is provided by the NOAA Climate Data Record Program (Knapp 2014). GridSat-B1 has data from January 1980 to the present for the entire globe. The data are at 3-hourly temporal resolution and 0.07° × 0.07° horizontal resolution. To map the satellite data into the equirectangular projection, the satellite pixel nearest the value of the latitude and longitude was selected (i.e., resampling). The version used in this analysis is v02r01, which was released in April 2014. We used the 11-μm infrared window channel, which is of climate data record quality; climate data record quality is defined as "a time series of measurements of sufficient length, consistency, and continuity to determine climate variability and change" (National Research Council 2004).

Environmental fields at 3-hourly time scales were obtained from the fifth generation ECMWF atmospheric reanalysis (ERA5) dataset of the global climate (Hersbach et al. 2020). Serra et al. (2023) showed that cloud coverage or flux calculation has significant biases when comparing ERA5 to the PISTON 2018 observations, but the wind data were in good agreement, and ERA5 data had smaller biases than other coarser reanalysis datasets. ERA5 reanalysis data are currently available from 1 January 1979 to the present. The gridded ERA5 reanalysis has a horizontal resolution of 0.25° × 0.25°. Monthly means of daily mean ERA5 data were utilized to create monthly climatologies.

For TC data, the location of the TC center and the TC's intensity were obtained from best track data from the International Best Track Archive for Climate Stewardship (IBTrACS) version 4 (Knapp et al. 2010, 2018). We used 3-hourly data (interpolated from 6-hourly data by IBTrACS) for TCs over the WNP from 1980 to 2019 for June–September. For the 40-yr period, there were 1392 TCs recorded in the WNP IBTrACS dataset, with 850 TCs in the WNP monsoonal area, defined as 0°–30°N and 100°–150°E.

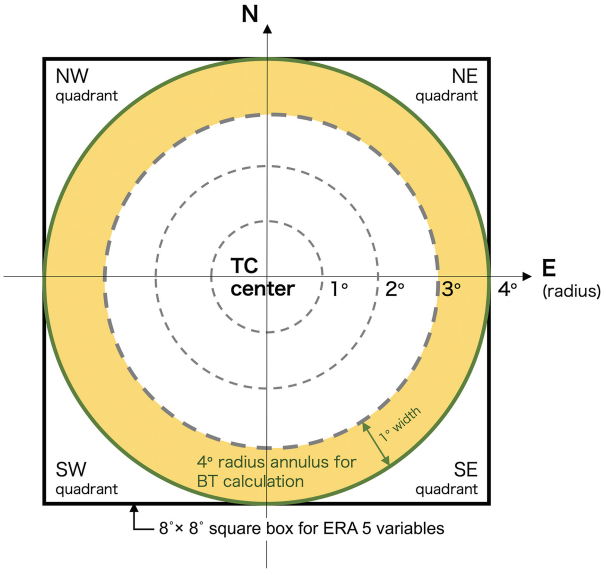

FIG. 2. A diagram of the methodology used to calculate infrared BT and environmental variables from ERA5 in our TC-centered analysis. BT data are taken as an annulus with 1° width, and ERA5 data are calculated using a square box. For example, for an analysis at 4° radius, BT grid points inside the yellow area are used, and ERA5 grid points spanning an 8° × 8° box are used.

The radar observation of Invest 98°W was obtained from the Colorado State University Sea-Going Polarimetric (SEA-POL) radar (Rutledge et al. 2019), which was mounted on the Research Vessel (R/V) *Thomas G. Thompson* for the PISTON field campaign. The SEA-POL radar is a polarimetric C-band (5.65 GHz) weather radar, ship and land deployable with a stabilized antenna system. During PISTON, we ran a scanning strategy combining an automatic 360° plan position indicator (PPI) volume scan and user-select range–height indicator (RHI) scans. Detailed descriptions of the scanning strategies implemented during PISTON and the extensive data quality-control processes can be found in Chudler and Rutledge (2021) and Chudler et al. (2022).

b. Methods

1) Data processing

Infrared brightness temperature (BT) was used as a proxy for deep convection, with colder BT values indicating higher cloud tops. We tracked the center of each TC using the IBTrACS track data in the western North Pacific bounded by 0°–30°N and 100°–150°E. We then take all of the GridSat-B1 grid points inside the 10° radius circle around the TC center to calculate two metrics: radial mean BT and radial convective coverage. Both metrics are calculated over an annulus using a 1° interval (Fig. 2). For example, the mean BT for the annulus at 4° radius means that all BT grid points inside an annulus

with a radius range from 3° to 4° are averaged. The BT data have 0.07° grid resolution, so 14 BT grid points fit in a 1° annulus. The innermost 0°–1° is a filled circle instead of an annulus.

At each 3-h interval, quadrant-averaged BT and 215-K convective coverage anomalies were calculated. Three-hourly ERA5 data were synced with the BT data. Winds at 200 and 850 hPa, vorticity, convergence, sea surface temperature (SST), relative humidity (RH), and total column water vapor (TCWV) were examined. Zonal vertical wind shear (U shear) and meridional vertical wind shear (V shear) were calculated as the wind difference between 200 and 850 hPa. Unlike BT data that were taken in an annulus shape, the wind data were averaged over a square box centered on the TC location at a specific time from the IBTrACS data. For example, matching with a 4° radius annulus of BT data is an 8° × 8° square of ERA5 data (Fig. 2). While ERA5 may contain positional errors in TC vortex centers, the use of best track positions and a relatively large averaging domain minimizes the impact of such discrepancies (Zarzycki et al. 2021).

For vertical wind shear calculations, various methods have been used in TC research, including vortex-removal techniques (e.g., Paterson et al. 2005) and annular averaging as in the Statistical Hurricane Intensity Prediction Scheme (SHIPS; DeMaria et al. 2005). In this study, we adopt a simple, storm-centered box-averaging approach without explicit vortex removal. In a sufficiently large box, the symmetric component of the storm-induced shear tends to cancel out (e.g., Paterson et al. 2005). A sensitivity analysis using an annular VWS calculation confirmed that our main conclusions are robust to the choice of shear estimation method.

To track the vortex center of developing systems in our case studies, the Okubo–Weiss parameter was calculated from ERA5 wind data:

$$W = S_n^2 + S_s^2 - \omega^2. \quad (1)$$

We found that the Okubo–Weiss parameter W is better than relative vorticity ω for tracking developing TCs in that it takes into account the normal strain S_n and the shear strain S_s so that the parameter measures the relative importance of rotation over deformation. Eddies in which vorticity dominates strain are denoted by a negative W. The Okubo–Weiss parameter has been frequently used to track tropical cyclogenesis (Dunkerton et al. 2009; Tang et al. 2020; Nam and Bell 2021).

2) Identification of monsoon tail rainbands

Monsoon tail rainbands were identified using the BT data, focusing on outer-core convective asymmetries, particularly in the southern flank of the TC, within a 5°–10° radius annular region around the TC center.

The convective coverage is calculated as the percentage of grid points that have a BT below a threshold over all of the grid points inside each annulus. The annulus area was divided into four quadrants—northeast (NE), northwest (NW), SW, and SE. Two metrics were computed every 3 h: 1) BT anomaly, defined as the deviation from the azimuthal (360° annular) mean at each radius, and 2) convective coverage anomaly, defined as the percentage of grid points within each quadrant with BT ≤ 215 K, relative to the annular-mean coverage.

We tested two different thresholds suggested by previous literature on tropical convection: the 215-K deep convection index of Fu et al. (1990) and the 225-K cold cloud index of Nakazawa (1988). The results were not sensitive to the different thresholds, and we consequently adopt the deep-convection threshold BT ≤ 215 K for all subsequent analyses to minimize contamination from nonconvective high clouds such as cirrus and anvil clouds, which typically exhibit BTs in the range of 245–215 K depending on region and cloud thickness (Stubenrauch et al. 2013).

We employed two complementary MT identification methods, referred to as MT ID methods 1 and 2, to assess the presence, strength, and environmental context of MT features.

(i) MT ID method 1: Lifetime-averaged quadrant asymmetry

The first method assesses persistent convective asymmetry throughout each TC's lifetime. The 5°–10° annulus was divided into the four quadrants. Two metrics were computed every 3 h: 1) the brightness temperature anomaly (relative to the azimuthal mean) and 2) the convective coverage anomaly, defined as the fraction of grid points with BT ≤ 215 K relative to the annular mean. These anomalies were then averaged over the entire TC lifetime.

A TC was classified as having a MT rainband if either the SW or SE quadrant exhibited a significant negative anomaly—defined as exceeding 5% of the maximum anomaly across the dataset—in either metric.

(ii) MT ID method 2: Time-resolved event detection with threshold sensitivity

The second method identifies discrete MT "events" by comparing southern and northern deep convective coverage at each 3-hourly interval. The convective area, using the same deep-convection threshold (BT ≤ 215 K), was calculated separately for the southern and northern halves of the annulus. A MT event was defined as a continuous period during which the southern coverage exceeded the northern by a specified area threshold for at least a specified duration.

We tested several threshold combinations to assess detection sensitivity. Area thresholds ranged from 5000 to 50 000 km^2, and duration thresholds ranged from 6 to 36 h. The 5000-km^2 and 6-h thresholds are consistent with prior studies of outer MCSs associated with TCs or African easterly waves using infrared satellite data (e.g., Lee et al. 2012; Ocasio et al. 2020). The larger thresholds are supported by the case of Typhoon Jebi (2018), whose trailing rainband associated with Invest 98°W persisted for 39 h and exceeded 50 000 km^2 in convective area. For each identified event, we recorded the duration, maximum convective area, and the corresponding TC and environmental conditions at the time of peak convection.

(iii) Limitations of BT-based monsoon tail tracking

While satellite BT is a widely used proxy for deep convection, this approach has notable limitations. First, BT represents

cloud-top temperature rather than vertical motion or precipitation. Thick cirrus or anvil clouds may be misidentified as deep convective cores, particularly in environments with strong shear. Studies comparing infrared BT with radar-derived vertical profiles have reported discrepancies in convective depth and structure (e.g., Yuan and Houze 2010; Feng et al. 2021; Zuluaga and Houze 2013).

Second, MT ID method 1 is based on lifetime-averaged quadrant anomalies and does not explicitly track individual convective features. Although correlation analyses relate the SW quadrant BT anomaly to environmental variables at each time step, these anomalies may not represent coherent rainband structures. The method captures anomalously located convection in the southern quadrants but does not guarantee it takes the form of a trailing rainband.

MT ID method 2 complements this by applying spatial and temporal thresholds, but it too does not assess the geometry of the convection. Detected features may include broad, amorphous MCSs or scattered convection rather than arced or spiral rainbands. Although long-duration and large-area criteria (e.g., >24 h and >50 000 km^2) help filter out short-lived, diurnal signals, no manual or automated verification of rainband morphology was performed. However, the definition of a "rainband" can vary across studies, particularly with respect to its structure, spatial extent, and dynamical origin (e.g., Didlake and Houze 2009; Moon and Nolan 2015a,b), which makes it challenging to define and detect rainbands objectively.

In summary, while our BT-based quadrant anomaly and event-tracking methods provide reproducible and scalable frameworks for identifying outer-core convective asymmetries, they do not guarantee strict morphological classification of rainbands. The methods are best interpreted as tools to isolate robust convective signals consistent with MT behavior in large TC datasets.

3) Environmental correlation analysis

To investigate under what environmental and TC conditions MT rainbands tend to develop and persist, correlation analysis was conducted. The 3-hourly SW quadrant BT anomaly was used as a continuous proxy for MT strength. Pearson correlation coefficients (Pearson 1895) were computed between this metric and key environmental and TC variables at various radii from the TC center. Statistical significance was assessed using the two-sided Student's t test (Student 1908).

We also tested alternative proxies in the supplemental material: 1) the 3-hourly southern quadrants' (SW and SE) BT anomaly, 2) lifetime-averaged BT anomaly for the SW quadrant from MT ID method 1, and 3) the maximum convective area of each event from MT ID method 2.

3. Climatology of monsoon tail rainbands

a. Composite convective asymmetry around TCs

To establish the climatological characteristics of MT rainbands, we analyzed deep convection associated with 850 TCs over the WNP monsoonal region (0°–30°N, 100°–150°E) during June–September 1980–2019. Deep convection was tracked using infrared BT, following the methods described in section 2.

Figure 3 presents BT anomalies for each quadrant of the TC-centered annulus, calculated as deviations from the azimuthal mean at each radius. On average, the southern quadrants—especially the SW—exhibit colder BTs than the northern quadrants, indicating stronger and deeper convection. The SW quadrant anomaly becomes more pronounced with increasing radius, reaching a maximum negative anomaly of approximately 20°C relative to the radial mean in the 8°–10° annulus. Near the TC center, BT anomalies cluster around zero, indicating more symmetric convection in the inner-core region.

A similar quadrant-dependent pattern emerges when using the deep convection coverage metric, defined as the percentage of each annulus covered by BT ≤ 215 K (Fig. 4). Again, the SW quadrant shows the strongest convective signal, followed by SE, NE, and NW quadrants. The largest asymmetries in convective coverage are found in the 4°–6° annulus. At larger radii (e.g., 8°–10°), the deep convective coverage declines across all quadrants due to the growing annular area, which dilutes the fractional contribution of deep convection.

The fact that enhanced convection in the SW quadrant appears in a 40-yr climate composite suggests that the MT rainband is a climatologically common feature for TCs in the WNP monsoonal region.

b. Climatological frequency of monsoon tail rainbands (MT ID method 1)

To quantify how frequently TCs exhibit anomalous convection consistent with a MT structure, we applied MT ID method 1 to all 850 TCs in our 40-yr dataset (1980–2019) over the monsoonal WNP domain (0°–30°N, 100°–150°E). Each TC was categorized based on which quadrant within the 5°–10° annular region exhibited the coldest lifetime-averaged BT anomaly or the largest deep convective coverage anomaly.

Figure 5 shows the annual counts of TCs grouped by the quadrant with the strongest anomaly in (Fig. 5a) mean BT and (Fig. 5b) convective coverage. TCs with no quadrant exceeding a significance threshold—defined as 5% of the maximum anomaly in each metric—are labeled as "symmetric" and shown in purple. The threshold values used were 0.38 K for mean BT anomaly (based on a dataset maximum of −7.54 K) and 0.46% for convective coverage anomaly (based on a maximum of +9.17%). Among the 850 TCs, 200 (24%) and 282 (33%) were categorized as symmetric using the mean BT anomaly and convective coverage anomaly metrics, respectively.

In both metrics, the majority of TCs exhibited anomalous convective activity in the southern quadrants, supporting the climatological prevalence of the MT rainband structure. Based on the mean BT anomaly metric, an average of 44.2% of TCs each year showed SW dominance and 18.3% showed SE dominance, totaling 62%. Using the convective coverage anomaly metric, 43.2% of TCs showed SW dominance and 26.2% showed SE dominance, again indicating that over two-thirds of TCs exhibited a southern convective asymmetry.

There was considerable interannual variability in the dominant quadrant. The annual percentage of SW-dominant TCs

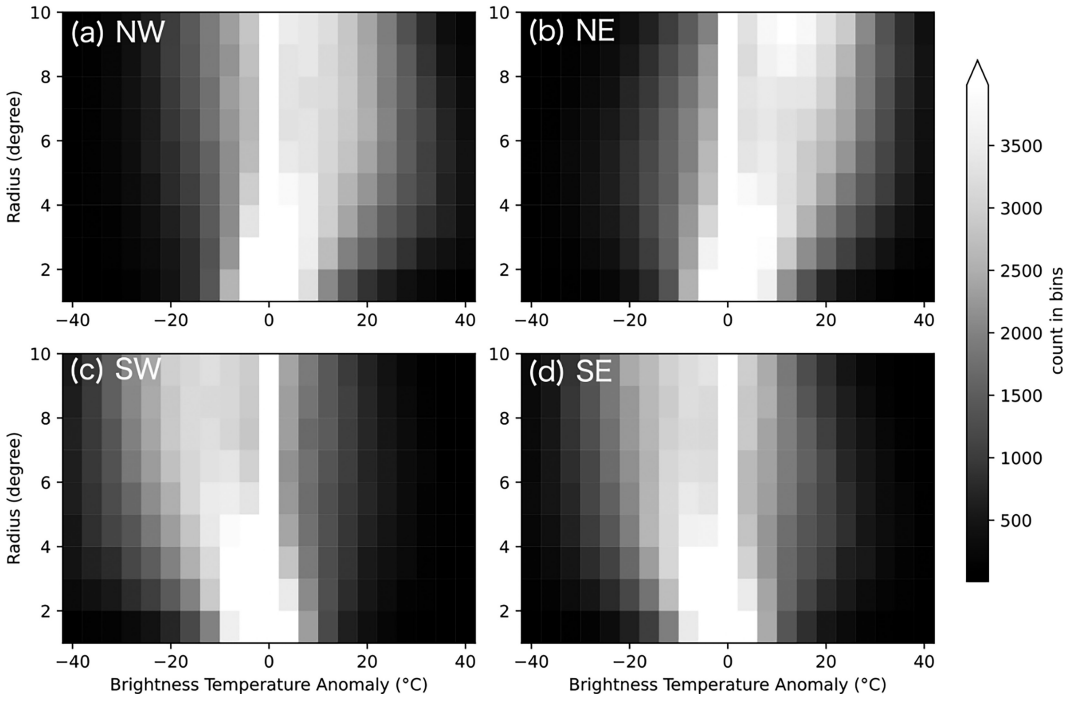

FIG. 3. The 2D histograms of infrared BT anomalies from the azimuthal (360° annular) mean, calculated for 3-hourly snapshots of TCs over 0°–30°N, 100°–150°E during June–September 1980–2019. Panels show BT anomalies by quadrant: (a) NW, (b) NE, (c) SW, and (d) SE. The x axis shows BT anomaly values (K), and the y axis shows radial distance from the TC center in degrees latitude (1° ≃111 km). Color shading indicates the number of grid points across all time steps falling within each BT anomaly and radius bin.

ranged from 19.2% to 68.4% based on the mean BT anomaly and from 26.9% to 63.2% based on the convective coverage anomaly. SE-dominant cases ranged from 4.2% to 41.7% (mean BT anomaly) and from 4.5% to 66.7% (convective coverage anomaly).

To explore potential drivers of this variability, we compared the annual frequency of SW-dominant TCs to the ENSO longitude index (ELI) (Williams and Patricola 2018) and the WNP monsoon index (Wang et al. 2008). Both indices showed modest correlations ($r \approx 0.3$–0.4) with MT frequency, with more pronounced tail features generally associated with stronger monsoon years and eastward-shifted ENSO phases. Full details and correlation plots are presented in Figs. S3 and S4.

c. *Frequency and structure of discrete monsoon tail events (MT ID method 2)*

To complement the lifetime-averaged perspective of MT ID method 1 and assess the occurrence and characteristics of individual MT events, we applied MT ID method 2 to the 850 TCs over the WNP from 1980 to 2019. As described in the methods section, we tracked the convective area with the same deep convection threshold (BT ≤ 215 K).

Figure 6 shows the joint distribution of MT event duration and deep convection area. Most events clustered between 6 and 24 h in duration and 5000–40 000 km^2 in maximum area (Fig. 6a), with fewer cases exhibiting both long duration and large convective extent. The southern-minus-northern area difference (Fig. 6b) exhibited a similarly shaped distribution because the northern convective area is generally small and less variable than the southern component. As a result, both metrics are largely controlled by variations in the southern convective area, with most events showing moderate south–north asymmetry and a substantial tail toward larger differences, reflecting stronger convective asymmetries favoring the southern quadrants. Three MT events associated with Super Typhoon Jebi (2018) are highlighted with red circles. The second event, characterized by a 39-h duration and a convective area exceeding 50 000 km^2, corresponds to the Invest 98°W episode that served as the initial motivation for this study.

Table 1 summarizes the number of TCs with MT events under various area and duration threshold combinations. Using the least stringent criteria (≥5000 km^2 and ≥6 h), 676 TCs (79.5%) exhibited at least one MT event. Across all 676 TCs, a total of 2219 MT events were identified over the 40-yr period, an average of 3.3 MT events per qualifying TC. As the detection criteria became more restrictive, the number of qualifying TCs decreased steadily. For example, only 155 TCs (18.2%) met the strictest criteria (area threshold of 50 000 km^2 and a duration threshold of 36 h), which align with the characteristics of Jebi's second MT event that was associated with Invest 98°W.

While this objective method enables reproducible identification of MT events across a large dataset, it does not explicitly evaluate the geometry or morphological structure of each

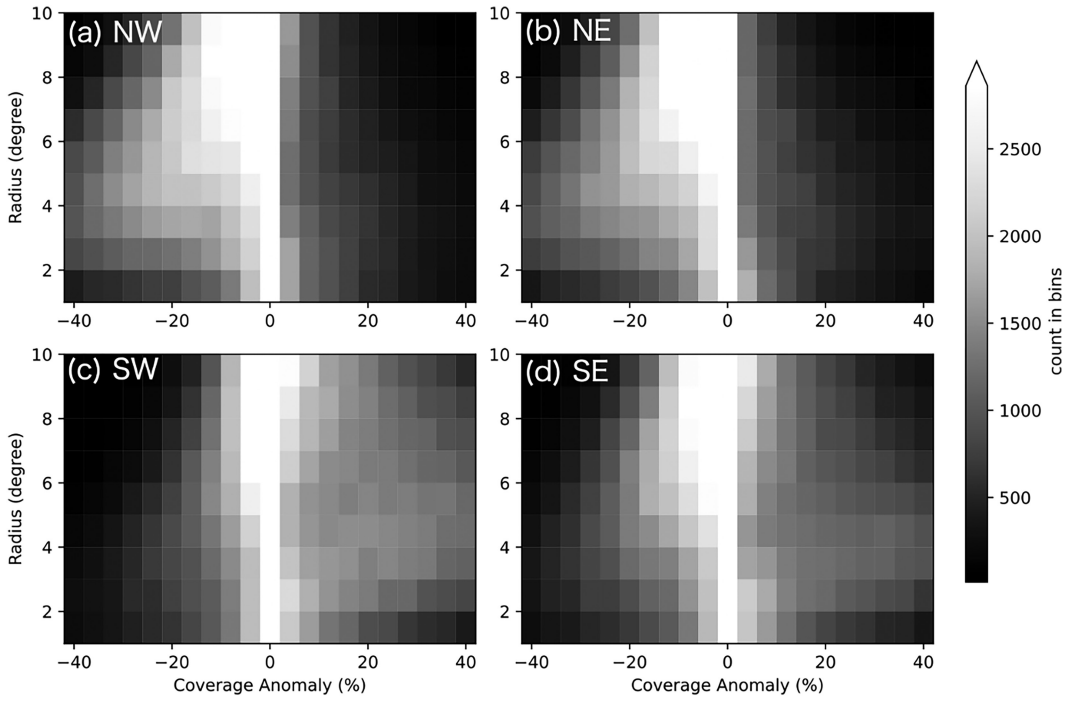

FIG. 4. As in Fig. 3, but for deep-convection coverage anomalies (BT ≤ 215 K) for each quadrant.

convective feature. Thus, some detected events—particularly those near the minimum area and duration thresholds—may not meet traditional definitions of spiral or arced rainbands. However, sensitivity tests using stricter thresholds consistent with meso-alpha scale and at least one diurnal cycle (i.e., ≥10 000 km and ≥24 h) confirm that a substantial subset of TCs (55.3%) still satisfy these more conservative criteria. These results suggest that large, long-lasting MT rainbands—like the one associated with Invest 98°W—are not rare features within the WNP monsoonal region.

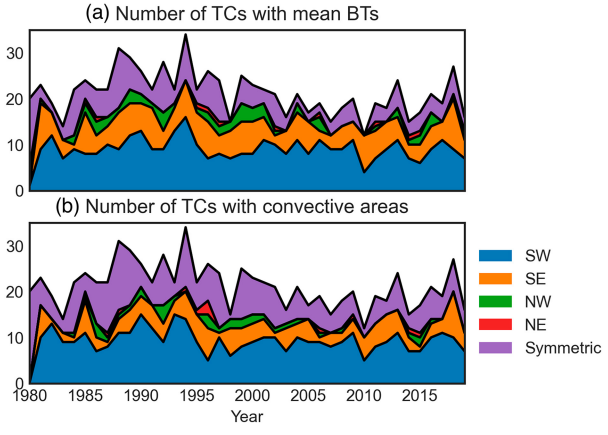

FIG. 5. Annual number of TCs in the WNP (June–September 1980–2019) grouped by the quadrant exhibiting the strongest convective anomaly within the 5°–10° annulus based on (a) mean BT and (b) deep convective coverage. Symmetric denotes cases where no quadrant exceeded the significance threshold.

4. Environmental and TC factors influencing monsoon tail rainbands

The preceding climatological analyses demonstrate that MT rainbands are not limited to the 2018–19 typhoon seasons of the PISTON field campaign but are instead a common feature of TCs over the WNP. These findings prompt the following research questions: What environmental- and storm-related factors are associated with the enhanced convection typically observed in the SW quadrant? Are these features organized primarily by the ambient monsoon southwesterlies? Or do they arise from TC characteristics, such as location or intensity?

To answer these questions, we calculated Pearson correlations between the mean BT anomalies in the SW quadrant as an MT rainband proxy with other environmental and TC variables at each radius (Fig. 7). These correlations are intended to diagnose large- to synoptic-scale environmental controls rather than localized mesoscale variability (e.g., convective instability). All 10 variables shown in Fig. 7 exhibit statistically significant correlations with the monsoon tail proxy at the 99% confidence level ($p < 0.01$), based on the two-sided Student's t test for the null hypothesis of zero correlation. The correlation generally increases with radius and saturates around 6° as the mean BT anomaly increases with radius (Fig. 3). Scatterplots of these 10 variables on the y axis and the SW BT anomaly on the x axis can be found in Fig. S5.

The strongest correlation was with zonal vertical wind shear (U shear, 200–850 hPa), exceeding 0.6 beyond 5° radius and explaining over 40% of the variance in SW BT anomalies. This positive correlation reflects that easterly shear (negative U shear) shifts convection toward the downshear, especially

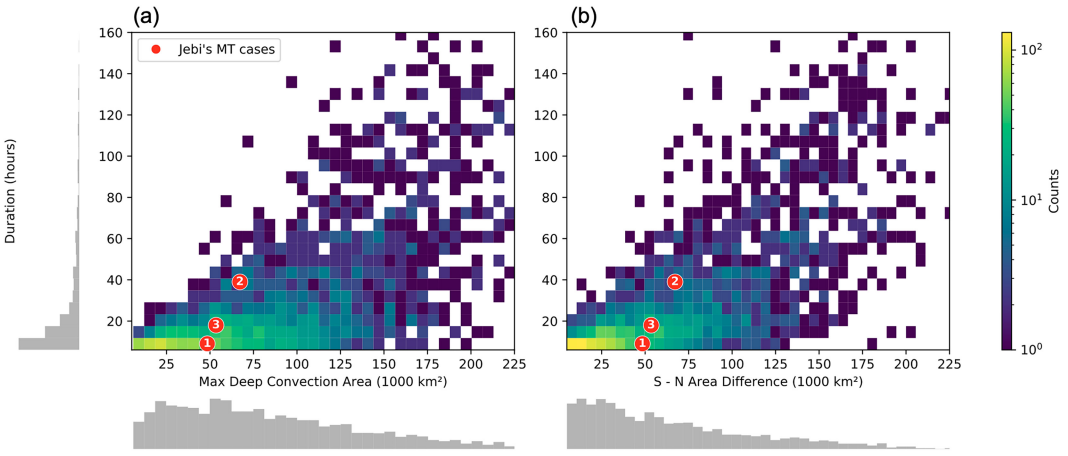

FIG. 6. Two-dimensional histograms of MT events detected using MT ID method 2 for 850 TCs over the WNP from 1980 to 2019, using a 6-h and 5000-km^2 threshold. (a) Maximum deep-convection area vs event duration. (b) Difference in deep-convection area between southern and northern annuli vs event duration. Color shading indicates event frequency on a logarithmic scale. Marginal 1D histograms for each axis are shown. Red circles highlight three MT events associated with Super Typhoon Jebi (2018), with the second event corresponding to the MT associated with Invest 98°W that motivated this study.

downshear-left quadrant (i.e., SW quadrant). This result is consistent with well-established findings on shear-induced convective asymmetries in tropical cyclones (Corbosiero and Molinari 2003; DeHart et al. 2014; Rios-Berrios 2020).

The next best correlation with the MT rainband feature is found in the meridional vertical wind shear (V shear) and U850 with magnitudes of correlation around 0.4. Negative V shear (northerly shear) acts to shift convection southward from the TC center (negative BT anomaly in the SW quadrant together). For U850, the correlation is negative, consistent with enhanced MT convection when low-level westerlies (positive U850) are stronger in the SW quadrant. Here, U850 should be interpreted as a measure of the zonal component of the low-level inflow into the MT region, combining contributions from both southwesterlies and northwesterlies on the western flank of the TC circulation, rather than as a pure proxy for southwesterly monsoon flow.

TABLE 1. Number of TCs with MT events for each area and duration threshold combination. Percentages in parentheses indicate the fraction of the total 850 TCs over the monsoonal WNP (0°–30°N, 100°–150°E) during June–September 1980–2019. The final column indicates the total number of MT events detected.

Duration threshold (h)	Area threshold (km^2)	TCs with events (%)	Total MT events
6	5000	676 (79.5%)	2219
6	10 000	663 (78.0%)	2179
6	20 000	627 (73.8%)	2086
6	50 000	530 (62.4%)	1567
12	5000	621 (73.1%)	1436
12	10 000	595 (70.0%)	1382
12	20 000	552 (64.9%)	1233
12	50 000	416 (48.9%)	828
24	5000	503 (59.2%)	743
24	10 000	470 (55.3%)	678
24	20 000	400 (47.1%)	558
24	50 000	227 (26.7%)	276
36	5000	418 (49.2%)	527
36	10 000	380 (44.7%)	474
36	20 000	318 (37.4%)	381
36	50 000	155 (18.2%)	169

Low-level convergence at 850 hPa exhibited weaker correlations with the MT proxy (approximately 0.2) than initially expected. Previous case studies have emphasized the role of low-level confluence between monsoonal flow and TC cyclonic circulation in organizing outer MCSs in the WNP (Chen et al. 2014a, 2016). The comparatively weak relationship in our composite analysis may stem from the localized and transient nature of this confluence zone, which may not be well resolved in the coarse-resolution reanalysis data or adequately represented in a statistical framework spanning many TCs. Thermodynamic variables of SST and TCWV also had correlations of 0.2, with higher SST and more TCWV correlated with an enhanced SW BT anomaly.

TC intensity and TC longitude also have significant but small correlations of 0.2 with the MT feature. Weaker TC intensity and a westward shift in TC location are all associated with an enhanced MT rainband. TC size (30-kt radius; 1 kt $\approx$ 0.51 m s^{-1}) has the least correlation with the MT feature. The correlation was even smaller when tested with the 50-kt radius.

Figure 8 shows the summertime climatology of WNP dynamic and thermodynamic fields. The zonally elongated band of enhanced 200-hPa divergence, 850-hPa vorticity, and 850-hPa relative humidity indicates the monsoon trough region. Around the monsoon trough region, there are northeasterlies at upper levels and southwesterlies at lower levels producing large northeasterly vertical wind shear (Fig. 8c). The climatological northeasterly VWS is consistent with the climatological convective asymmetry in the SW quadrant of TCs. Thus, the convective

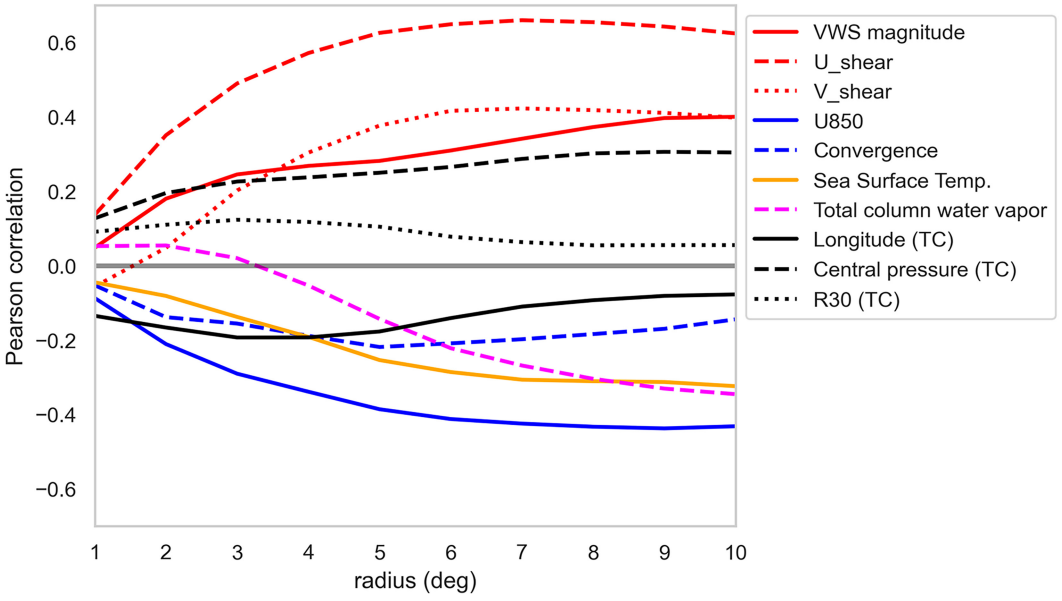

FIG. 7. Pearson correlation coefficients between the SW quadrant BT anomaly and various environmental and TC variables, shown as a function of radius from the TC center. VWS variables (200–850 hPa) are shown in red: total VWS magnitude, zonal wind shear (U shear), and meridional wind shear (V shear). Low-level (850 hPa) wind variables are shown in blue: zonal wind (U850) and convergence. SST and TCWV are in orange and magenta, respectively. TC-related variables are shown in black: longitudinal position of the TC center, minimum sea level pressure (intensity), and 30-kt wind radius (R30).

asymmetry in the SW quadrant of TCs over the monsoonal region in the WNP can be at least partly explained by the climatological northeasterly VWS. The positive relationship between the westward shift in longitude and the MT rainband can also be explained by the wind field. The direction of the low-level winds changes around 130°–140°E, with low-level southwesterly flow farther west and easterly trade wind flow farther east. Between 110° and 150°E, the farther west a TC tracks, the greater the chance for the TC to experience larger northeasterly VWS, favoring the development of a MT rainband feature. While we did not analyze other TC basins, we infer that MT features are unlikely in the Atlantic and eastern North Pacific due to differing climatological VWS patterns (Finocchio and Majumdar 2017).

If MT rainbands were primarily driven by low-level convergence at the confluence of the TC's cyclonic flow and the monsoon southwesterlies, one might expect stronger TCs—with more robust outer northwesterly winds—to produce greater convergence in the SW quadrant. However, our correlation analysis shows only a weak relationship between MT intensity and TC intensity and no meaningful relationship with TC size, suggesting that other mechanisms play a more dominant role. This is consistent with our broader findings that VWS, particularly the shear-relative configuration of low-level inflow and upper-level outflow, exerts a stronger influence on MT rainband development. Stronger TCs tend to resist shear-induced asymmetries, maintaining a more axisymmetric structure (e.g., Fischer et al. 2022), while weaker TCs are more vulnerable to shear and more likely to exhibit downshear-enhanced convection consistent with MT structures. Additionally, the role of frictional convergence arising from wavenumber-1 vorticity asymmetries in sheared TCs, as described by Riemer (2016), may also contribute to the convective asymmetries.

To further explore these associations, we conducted additional correlation analyses using alternative MT proxies, including mean BT anomalies in the broader southern quadrants (i.e., both SW and SE; Fig. S6) and the maximum convective area of each MT event identified by MT ID method 2 (Fig. S7). The results using the southern quadrant BT anomaly were generally consistent with Fig. 7, though the correlation with V shear was slightly stronger, while the correlation with TC longitude was weaker. Correlations using the maximum convective area were overall weaker than those using the 3-hourly BT anomalies (cf. Figs. S5 and S7), with the highest coefficients (around 0.3) again found for V shear. Notably, larger MT events tended to be associated with stronger vertical wind shear (both northerly and easterly components), as well as higher SST and total column water vapor over the $16° \times 16°$ area surrounding the TC center. Regarding TC size, we found no relationship between mean BT anomaly and the 30-kt wind radius. However, a weak but statistically significant relationship ($R^2 = 0.03$) emerged when using the maximum MT convective area as the proxy. This suggests that larger and longer-lived MT events are modestly associated with larger TCs. This finding aligns with Chen et al. (2014b), who showed that among all the outer MCSs south of the WNP TCs, only the broader and longer-lived convective system, which they called "enhanced rainbands," had impacts of expanding the TC size.

Taken together, these correlation analysis results suggest that enhanced SW convection—characteristic of MT rainbands—is more strongly influenced by vertical variations in the monsoonal wind field (i.e., vertical wind shear) than by low-level

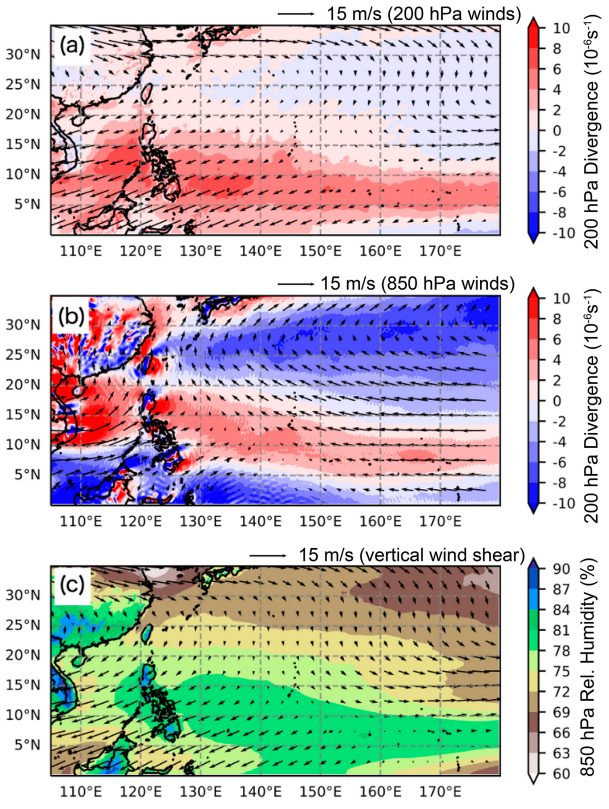

FIG. 8. The 40-yr summertime (June–September) climatology of (a) divergence and winds at 200 hPa, (b) relative vorticity and winds at 850 hPa, and (c) RH at 850 hPa and deep-layer (200–850 hPa) VWS over the WNP.

monsoonal flow alone (Fig. 7 and Fig. S6). These findings are consistent with recent studies examining shear-relative low-level flow and its role in modulating convective asymmetry in vertically sheared tropical cyclones, including idealized simulations (Chen et al. 2019) and climatological analyses (Chen et al. 2021). These studies demonstrate that low-level inflow directed toward the downshear-left quadrant promotes the formation of asymmetric convective structures and can contribute to TC size expansion. For TCs embedded in the WNP monsoon trough, the prevailing background flow consists of northeasterly VWS and southwesterly low-level monsoonal inflow (see Fig. 8). This configuration results in low-level flow that is oriented approximately upshear, a setup that favors convective enhancement in the downshear-left quadrant—typically the SW quadrant. Such a mechanism likely contributes to the observed climatological preference for SW quadrant convection and the formation of MT rainbands in WNP TCs.

5. Subsequent tropical cyclogenesis from monsoon tail rainbands

a. *Invest 98°W: A detached monsoon tail rainband with genesis potential*

To investigate TCG seeded by MT rainbands, we analyzed the 2018 case of Typhoon Jebi during the PISTON field campaign in greater detail. Jebi's MT rainbands exhibited convective features comparable to those of the inner core that later became isolated from the TC and remained in the monsoonal flow while Jebi moved northward. This detached rainband evolved into a widespread convective system that developed a distinct low-level circulation, subsequently tracked by the JTWC as Invest 98°W.

Figure 9 illustrates the evolution of the low-level wind field and the Okubo–Weiss parameter for Jebi and Invest 98°W. Initially, the region was dominated by weak southwesterlies, but Jebi's approach enhanced and extended the flow farther eastward. Invest 98°W developed a localized low-level circulation around 13°N, 138°E, approximately 10° away from Jebi, by 1200 UTC 2 September 2018, shown as curved streamlines and elevated Okubo–Weiss (OW) values in Fig. 9c. Vorticity remained collocated within the convection between 0000 and 1200 UTC 3 September before convection dissipated on 4 September. Even after the convection dissipated, the low-level circulation persisted for several days (Figs. 9f–h).

Figure 10 shows time series of thermodynamic and dynamic variables averaged inside a 5° × 5° box centered at 16.5°N, 138°E—the location of Invest 98°W. The thermodynamic environment around Invest 98°W was favorable throughout the tracking time, with SST above 29°C and TCWV close to 60 mm from 1200 UTC 2 September 2018 until it dissipated around 1200 UTC 4 September. Convective coverage peaked around 1200–1500 UTC [21–00 local time (LT)] 2 September, and then from the morning of 3 September, convective activity was muted at this location. For tropical oceanic convection, scattered and isolated convection does not have a clear diurnal cycle, but mesoscale convection shows a clear nocturnal maximum for radiative cooling of the upper troposphere (Nesbitt and Zipser 2003; Yang and Slingo 2001).

Relative vorticity at this location began increasing as convective coverage declined in the morning of 3 September, peaked at 0600 LT 3 September (2100 UTC 2 September), and sustained until around 0000 UTC 4 September (black line in Fig. 10). The period of increased vorticity coincided with strengthening northeasterly upper-level winds, connected to Jebi's outflow (Fig. S2). The combination of Jebi's large wind field and monsoonal flow sets up a synoptic background for increased vorticity; however, vorticity can be generated locally through vortex stretching in deep convection and persist within an insulated wave pouch even after convection has dissipated (e.g., Nam and Bell 2021; Smith et al. 2021).

Figure 11 presents the vertical structure of the Invest 98°W vortex tower (the vertically aligned column of cyclonic vorticity) during the period when it exhibited a closed low-level circulation collocated with widespread convection using ERA5 data (Fig. 9b). Invest 98°W experienced strong northeasterly vertical wind shear (>16 m s^{-1} for the 200–850-hPa deep-layer shear, indicated by red contours in Fig. 11), accompanied by dry air. This northeasterly VWS appears to originate from the anticyclonic upper-level outflow of Typhoon Jebi (see Fig. S2). Despite possessing strong core vorticity, Invest 98°W's vortex tower was significantly impacted by the VWS, with shear between 600 and 700 hPa reaching approximately 10 m s^{-1}. This pronounced tilt resulted in a truncated vortex tower in the latitude–height view at 138°E, extending vertically

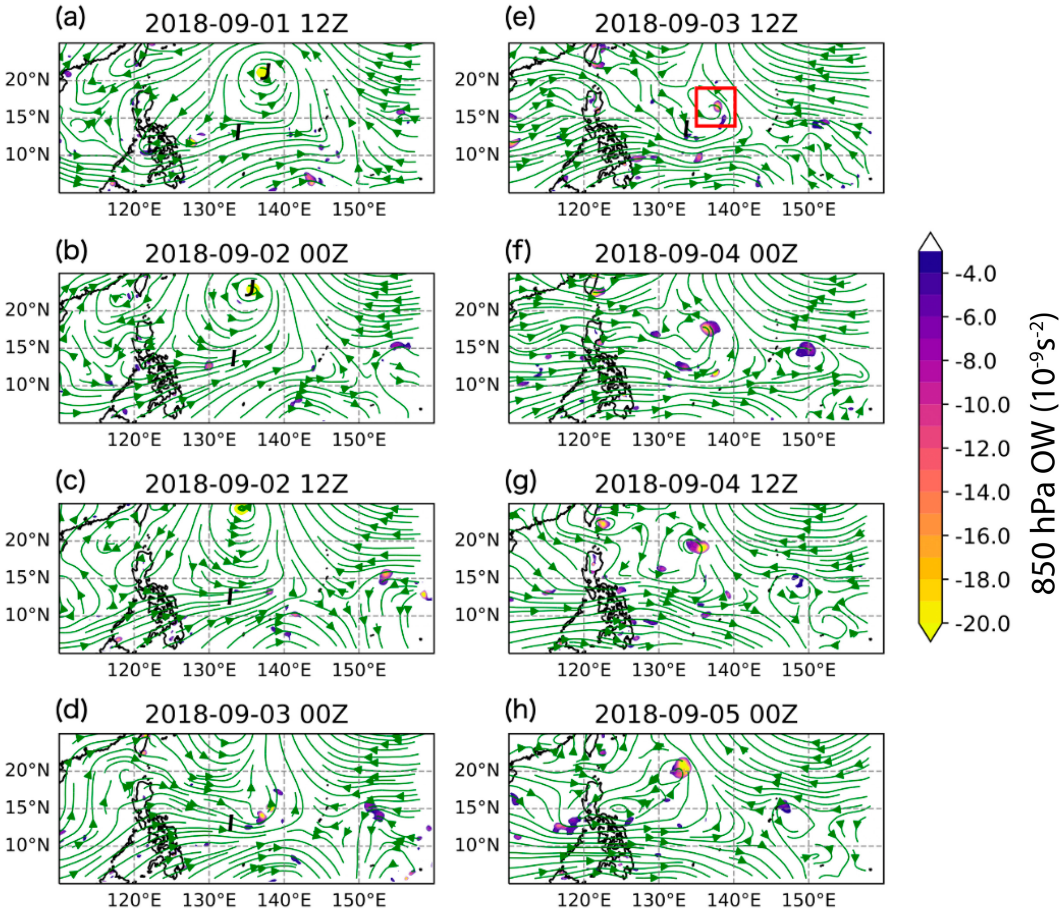

FIG. 9. OW parameter and streamlines at 850 hPa from 12-hourly ERA5 analyses between 1200 UTC 1 Sep 2018 and 0000 UTC 5 Sep 2018. The letter "*J*" denotes the location of Super Typhoon Jebi, and "*I*" marks the broad convective region associated with Invest 98°W (see also Fig. 1). The red 5° × 5° box in (b) denotes the region used to compute the time series in Fig. 10. The zonal and meridional cross sections in Fig. 11 are extracted through the center of this box at 16.5°N and 138°E, respectively.

only up to 700 hPa (Fig. 11a). From these observations, we conclude that strong VWS was likely the limiting factor for further development of Invest 98°W, despite favorable thermodynamic conditions and widespread convection near the low-level circulation of the detached rainband. Moreover, this VWS was partially produced by the outflow of the preexisting Typhoon Jebi. Jebi's circulation, therefore, both produced the MT rainband and led to its eventual demise.

b. *Mesoscale structure from SEA-POL radar observations*

Since the ERA5 and GridSat data can average out the localized signals from low-level wind and vertical convective structure, we examined the PISTON field campaign data; although the R/V *Thompson* was located approximately 5° away from the Invest 98°W location, the field observations provide more accurate, high-resolution insights. Radiosonde data from the R/V *Thompson* recorded 35–40-kt gusts associated with Invest 98°W, which also produced over 200 mm of rainfall within the SEA-POL shipborne radar domain from 2 to 3 September 2018. Figure 12 illustrates the convective structure of Invest 98°W observed by the SEA-POL radar. At 0000 UTC 3 September 2018, reflectivity images revealed a west-southwest–east-northeast (WSW–ENE) linear convective system embedded in stratiform precipitation (Fig. 12a) and near-surface westerlies of 15 m s^{-1} (Fig. 12b). Convection extending up to 12 km in echo-top height, at the 90-km range southeast of the SEA-POL (Fig. 12c), showed low-level convergence around 3-km altitude in RHI cross sections (Fig. 12d). Yu et al. (2018, 2023), using radar analyses of TCs near Taiwan, found that many outer rainbands originate from localized cold-pool-driven squall-line processes, which are consistent with the linear, rear-stratiform structure and low-level convergence observed in this case. Increased spectrum width in the convective region indicates local shear and turbulence (Fig. 12e). Local low–midlevel VWS may aid the upscale growth of convective systems in a developing tropical cyclone (Davis 2015; Nam and Bell 2021). While the climatological analyses above highlight strong correlations between MT features and environmental VWS, this case underscores the crucial role of low-level winds, both from

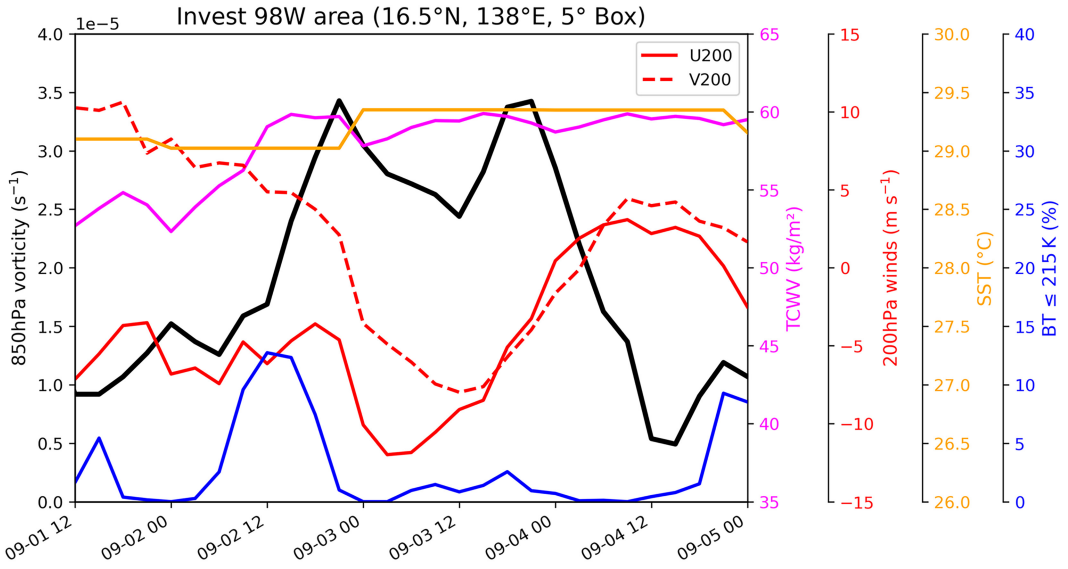

FIG. 10. Time series of TCG-related variables from 1200 UTC 1 Sep 2018 to 0000 UTC 5 Sep 2018, averaged within a 5° × 5° box centered at 16.5°N, 138°E—the location of Invest 98°W. Variables are derived from 3-hourly ERA5 reanalysis and GridSat data. Shown are 850-hPa relative vorticity (black), TCWV (magenta), 200-hPa winds (red), SST (orange), and deep-convection coverage (blue), defined as the percentage of the area with IR BTs ≤ 215 K.

monsoon westerlies and cyclonic winds from the circulation, in producing mesoscale convective organization. This radar analysis suggests that small-scale low–midlevel processes may be underrepresented by our synoptic-scale statistical analysis of MT events, as mentioned in the previous section.

c. *Climatological inhibition of secondary tropical cyclogenesis*

Although Invest 98°W did not successfully develop into a TC, we investigated whether other TCG cases could be seeded by MT rainbands. Using BT and TC track data, we manually examined all TCG events south of a preexisting TC in the monsoon southwesterly regime over the WNP for the 40-yr period. Only a few potential cases were identified through this subjective analysis. Most TCG events were instead associated with ITCZ or monsoon trough breakdowns producing multiple TCs simultaneously, such as Brendan, Caitlin, and Doug (1994). Others were linked to vortex Rossby wave energy dispersion (Li and Fu 2006), as observed in the cases of Jelawat and Ewiniar (2000). No clear evidence was found of MT rainbands

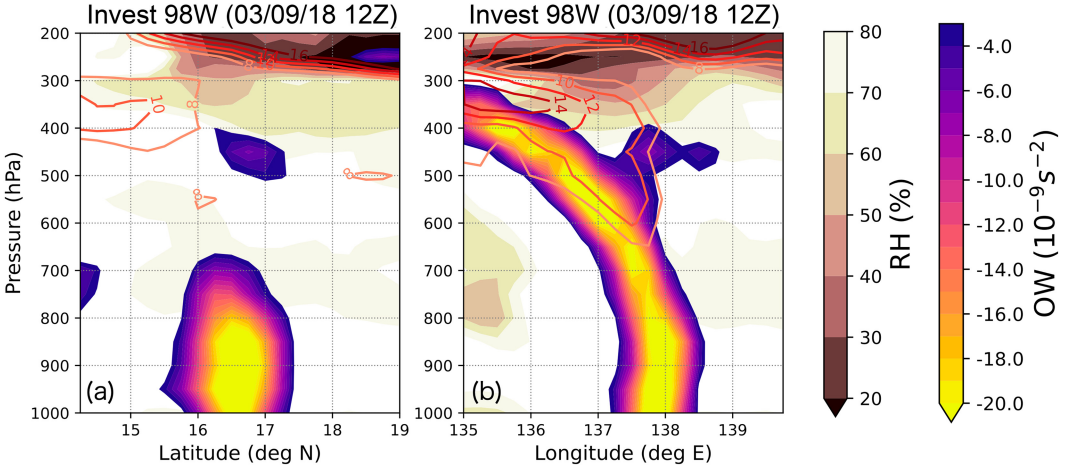

FIG. 11. Meridional and zonal cross sections of the vortex tower of (a),(b) Invest 98°W at 1200 UTC 3 Sep 2018—the time when Invest 98°W had the best chance of development with a closed low-level circulation inside the widespread convective area. The OW parameter and RH are in color, and VWS calculated between 850 hPa and each vertical level is in red contours in a range of 8–16 m s^{-1} magnitude from light red to dark red. The location of the 5° × 5° box is marked with red squares in Figs. 9.

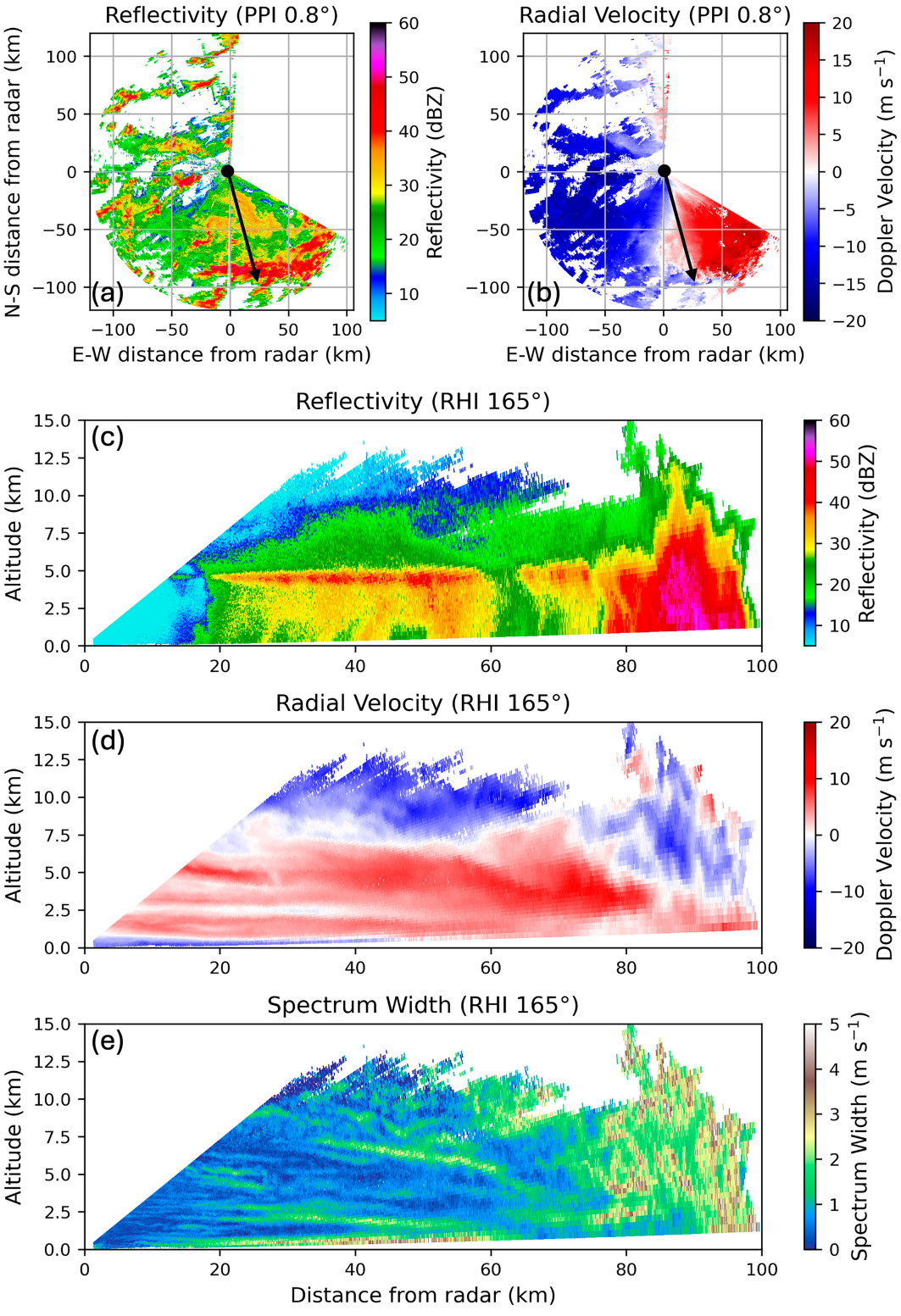

FIG. 12. Invest 98°W convection observed by SEA-POL. (a),(b) PPI top–down views of reflectivity and radial velocity at 0.8° elevation (0015:21 UTC 3 Sep 2018). (c)–(e) RHI vertical cross sections of reflectivity, radial velocity, and spectrum width at 165° azimuth (0010:46 UTC 3 Sep 2018). Black arrows in (a) and (b) mark the cross-sectional location in (c)–(e). The blank sector in the PPIs is due to SEA-POL's nontransmission over a 120° sector around the ship bridge.

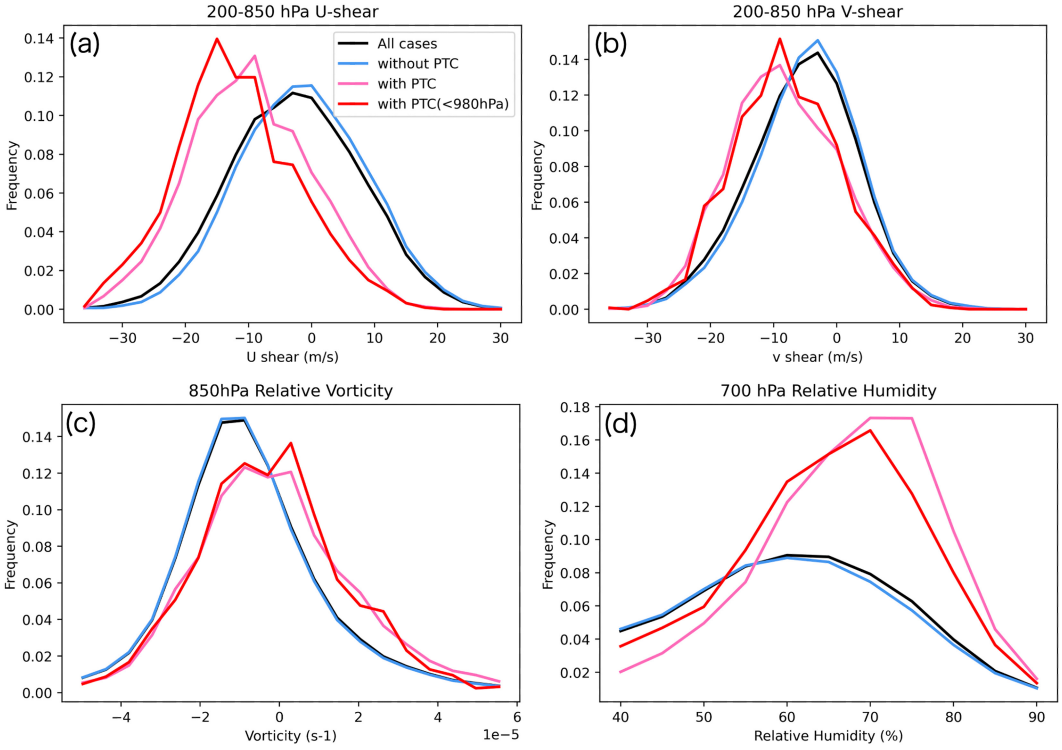

FIG. 13. PDF of (a) zonal VWS, (b) meridional VWS, (c) 850-hPa relative vorticity, and (d) 700-hPa RH at 16.5°N, 138°E (Invest 98°W's location at peak intensity at 1200 UTC 3 Sep 2018) for June–September 1980–2019. The black line represents the seasonal mean of all 3-hourly data at this location. The blue line shows cases without a PTC within 10° to the north, while the pink line indicates cases with a PTC within this range. The red line highlights a subset of the pink group where the PTC is intense (sea level pressure < 980 hPa).

directly leading to subsequent TCG except for TD19 in 2019, which originated from Typhoon Lingling. However, TD19 dissipated at the tropical depression stage (maximum sustained wind of 29 kt and minimum central sea level pressure of 996 hPa) due to strong northerly VWS (>15 m s^{-1}) associated with Lingling's outflow (not shown). The case of TD19 and Lingling provides a similar scenario to that of Invest 98°W and Typhoon Jebi.

We further investigated how the presence of a tropical cyclone to the north affects a hypothetical TCG scenario in the summer monsoon westerly regime of the WNP. Using Invest 98°W's location at its peak intensity (16.5°N, 137.9°E, 1200 UTC 3 September 2018; Fig. 11) as an illustrative example of TC genesis in the monsoon trough (Fig. 8), we calculated the climatological spectrum of VWS, low-level relative vorticity, and humidity. These calculations were based on whether a PTC was located within a 10° radius to the north, with results presented as probability density functions (PDFs) in Fig. 13.

The presence of a PTC to the north significantly intensifies easterly and northerly VWS at the hypothetical TCG location (Figs. 13a,b). Without a PTC, the mean VWS is near zero, reflecting the seasonal mean of all 3-hourly ERA5 data. In contrast, cases with a PTC show a mean zonal VWS of −15.8 m s^{-1}. Stronger PTC intensity further amplifies VWS (red vs pink lines), supporting the hypothesis that a PTC's outflow enhances VWS, since stronger TCs typically exhibit stronger outflows. Interestingly, the presence of a PTC also increases low-level vorticity and humidity (Figs. 13c,d), creating a more favorable environment for convective development. Statistically, the differences in means between the pink line and both the black and blue lines are significant ($p < 0.01$, t test), as are the differences between the pink and red lines for all variables except V shear ($p = 0.60$).

These factors could support systems like Invest 98°W—a long-lived mesoscale convective system with genesis potential. However, the negative impact of intensified VWS associated with the PTC outweighs these positive contributions and ultimately inhibits subsequent tropical cyclogenesis.

Based on the Invest 98°W case study and our climatological analysis, we conclude that the likelihood of TCG from MT rainbands is low. While the presence of a PTC enhances low-level vorticity and moisture that can promote convection, the PTC outflow generates unfavorable VWS which counteracts these positive effects and inhibits subsequent TC development.

6. Conclusions

This study investigated the monsoon tail (MT) rainband, an outer-core, southwestward-elongated region of widespread deep convection that were frequently observed during the 2018–19 PISTON field campaign. We analyzed its climatological behavior using 40 years of satellite and reanalysis data

over the western North Pacific (WNP) monsoonal region. We addressed the following research questions: 1) How common is it for TCs in the WNP to exhibit an elongated MT convective area (i.e., MT rainband)? 2) Under what environmental and TC conditions do such MT rainbands tend to develop and persist? 3) How common and likely is it for the MT rainband to lead to subsequent tropical cyclogenesis (TCG)?

To assess the frequency of MT rainbands, we introduced two complementary methods. MT ID method 1 used lifetime-averaged quadrant anomalies to capture persistent asymmetries, while MT ID method 2 applied time-resolved thresholds on convective area and duration. Using method 1, over 60% of TCs exhibited stronger convective activity in the SW or SE quadrants. Method 2, under a 6-h duration and 5000-km^2 area threshold, identified at least one MT event in 676 of 850 TCs (79.5%)—with over 2200 total events detected. Even under more conservative thresholds (e.g., ≥24 h and ≥10 000 km^2), over half of the TCs still qualified. These results confirm that mesoscale, long-lived MT rainbands are a common, climatologically robust feature in the WNP monsoonal environment.

To explore the factors influencing MT development, we examined both environmental conditions—such as wind shear, low-level flow, and thermodynamic fields—and storm characteristics, including TC location, intensity, and size. We performed correlation analyses using multiple metrics for MT strength. Zonal vertical wind shear (U shear) showed the strongest relationship with MT convective anomalies, explaining over 40% of the variance in the 3-hourly SW quadrant brightness temperature. Other significant but weaker correlations were found for meridional shear (V shear), low-level zonal wind (U850), and TC characteristics such as longitude and intensity. These findings highlight the role of the climatological northeasterly shear in the WNP in shaping convective asymmetries. While prior case studies (e.g., Chen et al. 2014a, 2016) have emphasized the role of localized low-level confluence zones in organizing outer-core convection, and although our SEA-POL radar observations of Invest 98°W also identified low-level convergence associated with linear MCS formation, our composite-based approach suggests that vertical shear is a more consistent large-scale predictor of MT occurrence.

The final question addressed the potential for MT rainbands to seed new tropical cyclones. We conducted a case study of Invest 98°W, a convective system that detached from Typhoon Jebi and developed a closed low-level circulation. The thermodynamic conditions around Invest 98°W were very favorable; however, development was ultimately suppressed by strong northeasterly vertical wind shear, amplified by Jebi's upper-level outflow. This dual role of the preexisting TC—both generating the MT rainband and inhibiting its further development—was echoed in another marginal case (TD19 from Typhoon Lingling in 2019). A climatological comparison of environments with and without a preexisting TC confirmed that preexisting TCs to the north not only enhance low-level vorticity and moisture but also strongly increase vertical wind shear, reducing the likelihood of TCG. Thus, MT rainbands—despite exhibiting large, persistent convection and closed circulations—rarely transition into tropical cyclones.

By combining climatological and case-based evidence, we show that MT rainbands are both frequent and impactful in the monsoonal area of the WNP. Their convective asymmetry is more strongly linked to the vertical structure of monsoonal wind patterns than to low-level flow alone. While they can display features resembling developing TCs, their proximity to a preexisting storm often creates hostile shear environments. These results contribute to the understanding the structure and evolution of outer-core convective systems and may aid in forecasting genesis potential in the monsoonal western North Pacific.

Acknowledgments. The authors express their gratitude to the scientists and engineers who contributed to the PISTON field campaign for their dedicated efforts in collecting the data utilized in this study. We also thank Phil Klotzbach, Brenda Dolan, and Eric Maloney for their valuable feedback on the early draft of this project. This research was supported by the Office of Naval Research under Awards N000141613033, N000142212737, and N000142012069.

Data availability statement. The PISTON observation datasets analyzed during the current study are available at the NASA data archive: https://www-air.larc.nasa.gov/cgi-bin/ArcView/camp2ex. The GridSat-B1, ERA5, and IBTrACS datasets analyzed in this study are reanalyses of existing data, which are openly available at locations cited in the reference section.

REFERENCES

Au-Yeung, A. Y. M., and C.-Y. Tam, 2018: Dispersion characteristics and circulation associated with boreal summer westward-travelling mixed Rossby–gravity wave–like disturbances. *J. Atmos. Sci.*, **75**, 513–533, https://doi.org/10.1175/JAS-D-16-0245.1.

Briegel, L. M., and W. M. Frank, 1997: Large-scale influences on tropical cyclogenesis in the western North Pacific. *Mon. Wea. Rev.*, **125**, 1397–1413, https://doi.org/10.1175/1520-0493(1997)125<1397:LSIOTC>2.0.CO;2.

Chen, B.-F., R. L. Elsberry, and C.-S. Lee, 2014a: Origin and maintenance of the long-lasting, outer mesoscale convective system in Typhoon Fengshen (2008). *Mon. Wea. Rev.*, **142**, 2838–2859, https://doi.org/10.1175/MWR-D-14-00036.1.

——, C.-S. Lee, and R. L. Elsberry, 2014b: On tropical cyclone size and intensity changes associated with two types of long-lasting rainbands in monsoonal environments. *Geophys. Res. Lett.*, **41**, 2575–2581, https://doi.org/10.1002/2014gl059368.

——, ——, and ——, 2016: Synoptic controls of outer mesoscale convective systems with high impact rainfall in western north pacific tropical cyclones. *Asia-Pac. J. Atmos. Sci.*, **52**, 11–23, https://doi.org/10.1007/s13143-015-0085-2.

——, C. A. Davis, and Y.-H. Kuo, 2019: An idealized numerical study of shear-relative low-level mean flow on tropical cyclone intensity and size. *J. Atmos. Sci.*, **76**, 2309–2334, https://doi.org/10.1175/JAS-D-18-0315.1.

——, ——, and ——, 2021: Examination of the combined effect of deep-layer vertical shear direction and lower-tropospheric mean flow on tropical cyclone intensity and size based on the ERA5 reanalysis. *Mon. Wea. Rev.*, **149**, 4057–4076, https://doi.org/10.1175/MWR-D-21-0120.1.

Chen, T.-C., and J.-H. Yoon, 2000: Interannual variation in Indochina summer monsoon rainfall: Possible mechanism. *J. Climate*, **13**, 1979–1986, https://doi.org/10.1175/1520-0442(2000)013<1979:IVIISM>2.0.CO;2.

——, S.-Y. Wang, M.-C. Yen, and A. J. Clark, 2008: Are tropical cyclones less effectively formed by easterly waves in the western North Pacific than in the North Atlantic? *Mon. Wea. Rev.*, **136**, 4527–4540, https://doi.org/10.1175/2008MWR2149.1.

Chudler, K., and S. A. Rutledge, 2021: The coupling between convective variability and large-scale flow patterns observed during piston 2018–19. *J. Climate*, **34**, 7199–7218, https://doi.org/10.1175/JCLI-D-20-0785.1.

——, ——, and B. Dolan, 2022: Unique radar observations of large raindrops in tropical warm rain during PISTON. *Mon. Wea. Rev.*, **150**, 2719–2736, https://doi.org/10.1175/MWR-D-21-0298.1.

Corbosiero, K. L., and J. Molinari, 2003: The relationship between storm motion, vertical wind shear, and convective asymmetries in tropical cyclones. *J. Atmos. Sci.*, **60**, 366–376, https://doi.org/10.1175/1520-0469(2003)060<0366:TRBSMV>2.0.CO;2.

Davis, C. A., 2015: The formation of moist vortices and tropical cyclones in idealized simulations. *J. Atmos. Sci.*, **72**, 3499–3516, https://doi.org/10.1175/JAS-D-15-0027.1.

DeHart, J. C., R. A. Houze, Jr., and R. F. Rogers, 2014: Quadrant distribution of tropical cyclone inner-core kinematics in relation to environmental shear. *J. Atmos. Sci.*, **71**, 2713–2732, https://doi.org/10.1175/JAS-D-13-0298.1.

DeMaria, M., M. Mainelli, L. K. Shay, J. A. Knaff, and J. Kaplan, 2005: Further improvements to the Statistical Hurricane Intensity Prediction Scheme (SHIPS). *Wea. Forecasting*, **20**, 531–543, https://doi.org/10.1175/WAF862.1.

Didlake, A. C., Jr., and R. A. Houze Jr., 2009: Convective-scale downdrafts in the principal rainband of Hurricane Katrina (2005). *Mon. Wea. Rev.*, **137**, 3269–3293, https://doi.org/10.1175/2009mwr2827.1.

Dunkerton, T. J., M. T. Montgomery, and Z. Wang, 2009: Tropical cyclogenesis in a tropical wave critical layer: Easterly waves. *Atmos. Chem. Phys.*, **9**, 5587–5646, https://doi.org/10.5194/acp-9-5587-2009.

Feng, Z., and Coauthors, 2021: A global high-resolution mesoscale convective system database using satellite derived cloud tops, surface precipitation, and tracking. *J. Geophys. Res. Atmos.*, **126**, e2020JD034202, https://doi.org/10.1029/2020JD034202.

Finocchio, P. M., and S. J. Majumdar, 2017: A statistical perspective on wind profiles and vertical wind shear in tropical cyclone environments of the Northern Hemisphere. *Mon. Wea. Rev.*, **145**, 361–378, https://doi.org/10.1175/MWR-D-16-0221.1.

Fischer, M. S., P. D. Reasor, R. F. Rogers, and J. F. Gamache, 2022: An analysis of tropical cyclone vortex and convective characteristics in relation to storm intensity using a novel airborne Doppler radar database. *Mon. Wea. Rev.*, **150**, 2255–2278, https://doi.org/10.1175/MWR-D-21-0223.1.

Fu, R., A. D. D. Genio, and W. B. Rossow, 1990: Behavior of deep convective clouds in the tropical Pacific deduced from ISCCP radiances. *J. Climate*, **3**, 1129–1152, https://doi.org/10.1175/1520-0442(1990)003<1129:BODCCI>2.0.CO;2.

Hersbach, H., and Coauthors, 2020: The ERA5 global reanalysis. *Quart. J. Roy. Meteor. Soc.*, **146**, 1999–2049, https://doi.org/10.1002/qj.3803.

Holland, G. J., 1995: Scale interaction in the Western Pacific Monsoon. *Meteor. Atmos. Phys.*, **56**, 57–79, https://doi.org/10.1007/BF01022521.

Knapp, K. R., 2014: NOAA Climate Data Record (CDR) of Gridded Satellite Data from ISCCP B1 (GridSat-B1) infrared channel brightness temperature, version 2. NOAA National Centers for Environmental Information, accessed 13 September 2020, https://doi.org/10.7289/V59P2ZKR.

——, M. C. Kruk, D. H. Levinson, H. J. Diamond, and C. J. Neumann, 2010: The International Best Track Archive for Climate Stewardship (IBTrACS). *Bull. Amer. Meteor. Soc.*, **91**, 363–376, https://doi.org/10.1175/2009BAMS2755.1.

——, H. J. Diamond, J. P. Kossin, M. C. Kruk, and C. J. Schreck III, 2018: International Best Track Archive for Climate Stewardship (IBTRACS) Project, Version 4. Data NOAA National Centers for Environmental Information, accessed 20 April 2020, https://doi.org/10.25921/82ty-9e16.

Lee, C.-S., B.-F. Chen, and R. L. Elsberry, 2012: Long-lasting convective systems in the outer region of tropical cyclones in the western North Pacific. *Geophys. Res. Lett.*, **39**, L21812, https://doi.org/10.1029/2012GL053685.

Li, T., and B. Fu, 2006: Tropical cyclogenesis associated with Rossby wave energy dispersion of a preexisting typhoon. Part I: Satellite data analyses. *J. Atmos. Sci.*, **63**, 1377–1389, https://doi.org/10.1175/jas3692.1.

Molinari, J., and D. Vollaro, 2013: What percentage of western North Pacific tropical cyclones form within the monsoon trough? *Mon. Wea. Rev.*, **141**, 499–505, https://doi.org/10.1175/MWR-D-12-00165.1.

Moon, Y., and D. S. Nolan, 2015a: Spiral rainbands in a numerical simulation of Hurricane Bill (2009). Part I: Structures and comparisons to observations. *J. Atmos. Sci.*, **72**, 164–190, https://doi.org/10.1175/JAS-D-14-0058.1.

——, and ——, 2015b: Spiral rainbands in a numerical simulation of Hurricane Bill (2009). Part II: Propagation of inner rainbands. *J. Atmos. Sci.*, **72**, 191–215, https://doi.org/10.1175/JAS-D-14-0056.1.

Nakazawa, T., 1988: Tropical super clusters within intraseasonal variations over the western Pacific. *J. Meteor. Soc. Japan*, **66**, 823–839, https://doi.org/10.2151/jmsj1965.66.6_823.

Nam, C. C., and M. M. Bell, 2021: Multiscale shear impacts during the genesis of Hagupit (2008). *Mon. Wea. Rev.*, **149**, 551–569, https://doi.org/10.1175/MWR-D-20-0133.1.

National Research Council, 2004: *Climate Data Records from Environmental Satellites: Interim Report.* The National Academies Press, 150 pp., https://doi.org/10.17226/10944.

Nesbitt, S. W., and E. J. Zipser, 2003: The diurnal cycle of rainfall and convective intensity according to three years of TRMM measurements. *J. Climate*, **16,** 1456–1475, https://doi.org/10.1175/1520-0442(2003)016%3C1456:TDCORA%3E2.0.CO;2.

Ocasio, K. M. N., J. L. Evans, and G. S. Young, 2020: Tracking Mesoscale Convective Systems that are potential candidates for tropical cyclogenesis. *Mon. Wea. Rev.*, **148**, 655–669, https://doi.org/10.1175/MWR-D-19-0070.1.

Paterson, L. A., B. N. Hanstrum, N. E. Davidson, and H. C. Weber, 2005: Influence of environmental vertical wind shear on the intensity of hurricane-strength tropical cyclones in the Australian region. *Mon. Wea. Rev.*, **133**, 3644–3660, https://doi.org/10.1175/MWR3041.1.

Pearson, K., 1895: VII. Note on regression and inheritance in the case of two parents. *Proc. Roy. Soc. London*, **58**, 240–242, https://doi.org/10.1098/rspl.1895.0041.

Riemer, M., 2016: Meso-β-scale environment for the stationary band complex of vertically sheared tropical cyclones. *Quart. J. Roy. Meteor. Soc.*, **142**, 2442–2451, https://doi.org/10.1002/qj.2837.

Rios-Berrios, R., 2020: Impacts of radiation and cold pools on the intensity and vortex tilt of weak tropical cyclones interacting with vertical wind shear. *J. Atmos. Sci.*, **77**, 669–689, https://doi.org/10.1175/JAS-D-19-0159.1.

Ritchie, E. A., and G. J. Holland, 1999: Large-scale patterns associated with tropical cyclogenesis in the western Pacific. *Mon. Wea. Rev.*, **127**, 2027–2043, https://doi.org/10.1175/1520-0493(1999)127<2027:lspawt>2.0.co;2.

Rutledge, S. A., V. Chandrasekar, B. Fuchs, J. George, F. Junyent, B. Dolan, P. C. Kennedy, and K. Drushka, 2019: SEA-POL goes to sea. *Bull. Amer. Meteor. Soc.*, **100**, 2285–2301, https://doi.org/10.1175/BAMS-D-18-0233.1.

Serra, Y. L., G. N. Kiladis, and M. F. Cronin, 2008: Horizontal and vertical structure of easterly waves in the Pacific ITCZ. *J. Atmos. Sci.*, **65**, 1266–1284, https://doi.org/10.1175/2007JAS2341.1.

——, S. A. Rutledge, K. Chudler, and C. Zhang, 2023: Rainfall and convection in ERA5 and MERRA-2 over the northern equatorial western Pacific during PISTON. *J. Climate*, **36**, 845–863, https://doi.org/10.1175/JCLI-D-22-0203.1.

Smith, R. K., G. Kilroy, and M. T. Montgomery, 2021: Tropical cyclone life cycle in a three-dimensional numerical simulation. *Quart. J. Roy. Meteor. Soc.*, **147**, 3373–3393, https://doi.org/10.1002/qj.4133.

Sobel, A. H., and C. S. Bretherton, 1999: Development of synoptic-scale disturbances over the summertime tropical northwest Pacific. *J. Atmos. Sci.*, **56**, 3106–3127, https://doi.org/10.1175/1520-0469(1999)056<3106:DOSSDO>2.0.CO;2.

——, J. Sprintall, E. D. Maloney, Z. K. Martin, S. Wang, S. P. de Szoeke, B. C. Trabing, and S. A. Rutledge, 2021: Large-scale state and evolution of the atmosphere and ocean during PISTON 2018. *J. Climate*, **34**, 5017–5035, https://doi.org/10.1175/JCLI-D-20-0517.1.

Stubenrauch, C. J., and Coauthors, 2013: Assessment of global cloud datasets from satellites: Project and database initiated by the GEWEX Radiation Panel. *Bull. Amer. Meteor. Soc.*, **94**, 1031–1049, https://doi.org/10.1175/BAMS-D-12-00117.1.

Student, 1908: The probable error of a mean. *Biometrika*, **6**, 1–25 https://doi.org/10.2307/2331554.

Takahashi, H. G., H. Fujinami, T. Yasunari, J. Matsumoto, and S. Baimoung, 2015: Role of tropical cyclones along the monsoon trough in the 2011 Thai flood and interannual variability. *J. Climate*, **28**, 1465–1476, https://doi.org/10.1175/JCLI-D-14-00147.1.

Tang, B. H., and Coauthors, 2020: Recent advances in research on tropical cyclogenesis. *Trop. Cyclone Res. Rev.*, **9**, 87–105, https://doi.org/10.1016/j.tcrr.2020.04.004.

Wang, B., Z. Wu, J. Li, J. Liu, C.-P. Chang, Y. Ding, and G. Wu, 2008: How to measure the strength of the East Asian summer monsoon. *J. Climate*, **21**, 4449–4463, https://doi.org/10.1175/2008JCLI2183.1.

Williams, I. N., and C. M. Patricola, 2018: Diversity of ENSO events unified by convective threshold sea surface temperature: A nonlinear ENSO index. *Geophys. Res. Lett.*, **45**, 9236–9244, https://doi.org/10.1029/2018GL079203.

Yang, G.-Y., and J. Slingo, 2001: The diurnal cycle in the tropics. *Mon. Wea. Rev.*, **129**, 784–801, https://doi.org/10.1175/1520-0493(2001)129<0784:TDCITT>2.0.CO;2.

Yoshida, R., and H. Ishikawa, 2013: Environmental factors contributing to tropical cyclone genesis over the western North Pacific. *Mon. Wea. Rev.*, **141**, 451–467, https://doi.org/10.1175/MWR-D-11-00309.1.

Yu, C.-K., C.-Y. Lin, L.-W. Cheng, J.-S. Luo, C.-C. Wu, and Y. Chen, 2018: The degree of prevalence of similarity between outer tropical cyclone rainbands and squall lines. *Sci. Rep.*, **8**, 8247, https://doi.org/10.1038/s41598-018-26553-8.

——, ——, and C.-H. Pun, 2023: Origin of outer tropical cyclone rainbands. *Nat. Commun.*, **14**, 7061, https://doi.org/10.1038/s41467-023-42896-x.

Yuan, T., and R. A. Houze Jr., 2010: Global variability of mesoscale convective system anvil structure from A-train satellite data. *J. Climate*, **23**, 5864–5888, https://doi.org/10.1175/2010jcli3671.1.

Zarzycki, C. M., P. A. Ullrich, and K. A. Reed, 2021: Metrics for evaluating tropical cyclones in climate data. *J. Appl. Meteor. Climatol.*, **60**, 643–660, https://doi.org/10.1175/JAMC-D-20-0149.1.

Zehr, R. M., 1992: Tropical cyclogenesis in the western North Pacific. Ph.D. thesis, Colorado State University, 189 pp.

Zuluaga, M. D., and R. A. Houze, 2013: Evolution of the population of precipitating convective systems over the equatorial Indian Ocean in active phases of the Madden–Julian oscillation. *J. Atmos. Sci.*, **70**, 2713–2725, https://doi.org/10.1175/JAS-D-12-0311.1.